Event-based Vision Sensor Physics-Based Digital Twin for Tuning SSA Use

Masashi Nishiguchi and Carolin Frueh
School of Aeronautics and Astronautics, Purdue University
mnishigu@purdue.edu,cfrueh@purdue.edu
Brian McReynolds
Institute of Neuroinformatics, UZH/ETH Zürich

ABSTRACT

Event-based vision sensors (EVS) are not frame-based and react to differential light on the single-pixel level. Their use has always been intriguing in space situational awareness problems. However, the need for the low magnitudes and high signal-to-noise ratios have been proving a challenge. Furthermore, non-linear time biases in the event registration do occur, thwarting precise astrometry. This paper presents a comprehensive physics-based simulation method for modeling the EVS pixel architecture. In contrast to other dynamic vision camera simulations, a truthful representation is found, avoiding rendering full frames to begin and without making broad simplifications. Specifically, the simulator incorporates the logarithmic photoreceptor, source follower buffer, change amplifier, and comparator. Each component's functionality is detailed, with a specific focus on the photoreceptor's response to light and thermal noise, the buffering and filtering processes, and the event generation mechanism. Key aspects of the simulation include the modeling of dark current as a Poisson process, the use of linear interpolation to handle the asynchronous nature of EVS data, and the incorporation of noise sources such as shot noise and leakage. A multi-pixel model is implemented to simulate the behavior of the entire sensor, allowing for the emulation of complex scenarios involving multiple moving targets. The simulator's accuracy is validated through qualitative and quantitative comparisons with real data from the DAVIS 346 sensor. The results demonstrate the simulator's capability to replicate the dynamic range and event-based data characteristics of the actual EVS, highlighting its effectiveness in evaluating sensor performance and optimizing bias configurations for Space Situational Awareness applications.

1. INTRODUCTION

Traditional frame-based cameras capture a series of images at a fixed frame rate and store them as video data. While this technology is widely used in daily life, as well as in academic and industrial settings, it has certain disadvantages. For instance, storing data for a pixel whose value does not significantly change over time is redundant. Additionally, important information can be missed between frames. In contrast, biological vision systems are event-driven and consist of cells that individually and asynchronously transmit information to the brain without forming a matrix of data at a fixed rate. Therefore, developing an engineering solution that incorporates biologically inspired, pixel-independent, and frame-free image acquisition techniques could address the limitations of frame-based cameras.

The first EVS was developed and reported in 2008 [8][9][10]. In an EVS, pixels are designed to react asynchronously to relative changes in brightness. Instead of generating images over time at a fixed rate, pixels in an EVS individually monitor whether the current brightness deviates from a memorized reference brightness by a specified threshold. The output of an event camera typically includes the time, pixel location, and polarity of each event. The polarity of an event indicates whether the change in brightness is positive (represented by 1) or negative (represented by -1). This approach allows event cameras to achieve high temporal resolution of approximately 1 s and a dynamic range of about 140 dB [4]. While the temporal resolution is not impressive on the single pixel, as the pixels act asynchronously and independently, motion can be captured almost continuously,

Due to the high temporal and spatial resolution of event cameras, researchers in the field of Space Situational Awareness (SSA) believe that these cameras can significantly advance their work. Chin et al. leveraged the event camera's low power consumption and high temporal resolution to develop an algorithmic pipeline for star tracking using event data [2]. Similarly, G. Cohen et al. conducted experiments and concluded that event cameras are well-suited for space-based SSA systems, owing to their low weight, low power consumption, and high temporal resolution [3].

However, since many effective image processing technologies in the field of Space Situational Awareness (SSA) rely on conventional frame-based data frameworks, the novel data structure of EVS presents a bottleneck for researchers aiming to integrate EVS into this field, with the initial works also showing significant draw-back of using EVS for SSA use. The problem of precise astrometry is still unsolved. Furthermore, timing biases have been observed, rendering the timing of the observations difficult, as traditional frame-time cannot be used. To address this challenge, researchers have developed simulators for EVS output, enabling them to explore potential applications without requiring access to the hardware itself. For example, V2E converts frame-based video data into EVS output by calculating the difference between brightness values in consecutive frames [6]. Benson and Holzinger approximated EVS pixel voltage using a first-order differential equation and simulated event rates for static point sources with both constant and time-varying mean brightness, as well as for moving sources [1]. Oliver and Salvansky proposed a physics-based EVS simulator tailored for SSA applications, incorporating satellite dynamics, atmospheric turbulence, and key elements of the V2E framework, particularly noise simulation [16]. Nevertheless, their algorithm for simulating photocurrent is not based on the underlying physics of a photodiode, and no quantitative validation of the simulation was provided. Therefore, this paper proposes an EVS simulator that takes incident photons as its input signal and generates events as output, making it more physics-based. Specifically, the simulator models the event output of the DAVIS 346, one of the most popular EVS models on the market, capturing the motion of five-point light sources that mimic the movement of objects in space as observed through a telescope. The model calculates the time history of photocurrent generated in a photodiode responding to the photon flux from the light sources, and then generates a list of events based on this time history. Additionally, linear interpolation of the photocurrent sampled at constant time intervals is implemented to preserve the asynchronous behavior of pixels in the EV sensor within the simulator.

2. SIMULATION METHOD

Figure 1 illustrates a typical EVS pixel design, which consists of four major components: the logarithmic photoreceptor, the source follower buffer, the change amplifier, and the comparator. In this section, we provide explanations of how each component functions and how it is modeled.

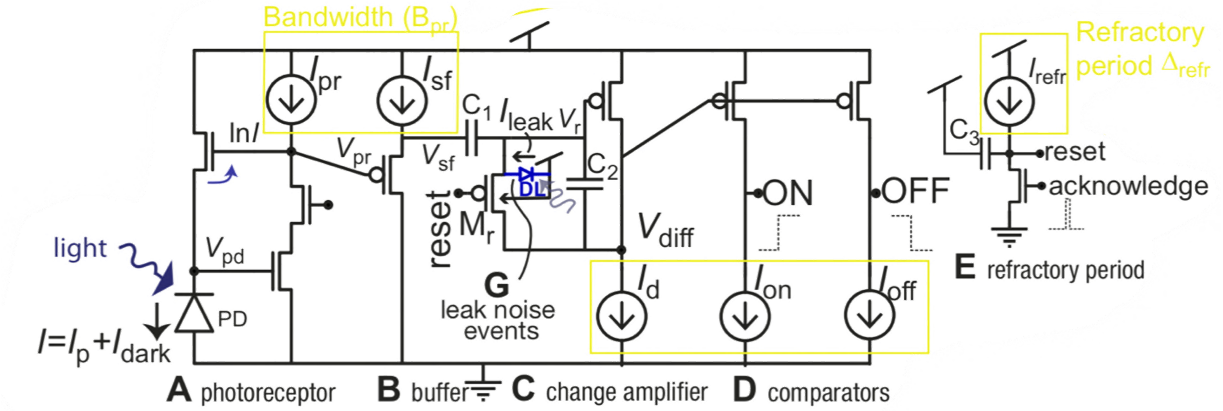

Fig. 1: Typical EVS pixel architecture (courtesy [5])

2.1 The Logarithmic Photoreceptor

The input signal of an EVS consists of photons in the form of light. When a photodiode is exposed to light, photons enter the semiconductor material. If the energy of these photons exceeds the material's bandgap energy, electron-hole pairs are generated, leading to a flow of free electrons, which we refer to as electric current. However, free electrons are generated not only by incident light but also by the thermal energy within the semiconductor material. The current generated by thermal energy is known as dark current, a significant source of noise in EVS under low illumination conditions. The total current generated by a photodiode can be expressed as shown in Equation 1, where I_p represents the current due to photon incidence, and I_{dark} represents the dark current. The dark current is calculated using the current density (J_{dark}), the total pixel area (A), and the fill factor (F), which is the ratio of the photodiode area to the total pixel area:

$$I = I_p + I_{dark} = I_p + J_{darl} AF \tag{1}$$

The amount of current a photodiode can generate from photon incidence depends on the material and geometrical properties of the photodiode. Equations 2 and 3 represent the photocurrent and dark current density, respectively, derived based on the physical phenomena occurring within a photodiode [7, 18]:

$$I_p = e\eta_i \tau\lambda \left(1 - \exp(-\alpha W)\right) \tag{2}$$

where τ is the transmission coefficient, α is the absorption coefficient, η_i is the internal quantum efficiency, λ is the incident photon rate, and e is the elementary charge.

$$J_{dark} = \left(\frac{eD_h}{L_h N_d} + \frac{eD_e}{L_e N_a}\right) n_i^2 + \frac{eWn_i}{\tau_g} \tag{3}$$

where D_h and D_e is the hole and electron diffusion coefficient, $L_{h,e}$ is the hole/ electron diffusion length, the N_a and N_d are the acceptor and dopant concentrations in a semiconductor, w is width of the depletion region, and n_i is the instrinsic concentration.

The advantage of the dark current model is that it is based on the actual phenomena occurring within a PD. However, most of the variables in the model are physical or material parameters specific to the PD implemented in the camera, and these details are often not publicly available. Consequently, while the model is precise in representing the actual phenomena, when it is used to model a specific sensor, the parameters need to be approximated based on the available information from other sensors with publicly accessible details.

Although the physical and material parameters for the PD used in the DAVIS 346 are not publicly available, iniVation, the manufacturer of the DAVIS 346, has reported that the average number of free electrons generated by thermal energy is $18000\,[e^-/\text{s}]$ [11]. Since the generation of free electrons due to thermal energy can be modeled by a Poisson process, the dark current at time t can be simulated by drawing a sample from a Poisson distribution with a mean of λ and multiplying it by the elementary charge as

$$I_{dark,\,t} = Pr[\lambda_{dark} = 18000] \times e \tag{4}$$

After the photocurrent is generated by the photon incidence, it is converted to a voltage that is proportional to the logarithm of the photocurrent, as shown in Equation 5. There are two advantages to the logarithmic relationship between the input light and the output voltage at V_{pr}. First, it compresses the output voltage, allowing the EVS to achieve a much higher dynamic range. Second, small changes around the background value become proportional to the background value. This means that the output signals for the same object under different lighting conditions are consistent to the first order [5]:

$$V_{pr} = \frac{U_T}{\kappa} \log\left(I_p + I_{dark}\right) \tag{5}$$

where U_T is the thermal voltage, and κ is the parameter of the transistor.

2.2 The Source Follower Buffer

The source follower buffer section acts as an intermediary between the highly sensitive logarithmic photoreceptor section and the spiking components, which include the change amplifier and comparator sections. In this part of the circuit, the noise component of the voltage signal, V_{pr}, which is faster than the signal of interest, is filtered out. This filtering process can be modeled as a first-order lowpass filter. The first-order lowpass filter is described by Equation 6, where S represents a general signal and f_c is the cut-off frequency.

$$S_{out}(t) = S_{in}(t) - \frac{1}{2\pi f_c}\frac{dS_{out}(t)}{dt} \tag{6}$$

Since the modeled input signal is discrete data, Equation 6 is discretized:

$$S_{out}(t_2) = 2\pi f_c \Delta t S_{in}(t_1) + (1 - 2\pi f_c \Delta t) S_{out}(t_1) \tag{7}$$

The cut-off frequency, f_c, is assumed to be a typical value of 10 [Hz]; however, in reality, it is controlled by the source follower bias current, I_{sf}.

2.3 The Change Amplifier

The change amplifier section (C in Figure 1) amplifies the filtered voltage, V_{sf}, by the negative ratio of the two capacitors, $-C_1/C_2$, resulting in V_{diff}. This process eliminates the DC component of V_{sf} [17].

2.4 The Comparators

The amplified voltage, V_{diff}, is continuously monitored and compared to the signal value at the last detected event, V_{ref}. If V_{diff} changes by the user-defined thresholds θ_{ON} or θ_{OFF}, an ON or OFF event is generated, and V_{ref} is updated to the value of V_{diff} at the time the event is detected. The ON and OFF thresholds are controlled by user-defined bias currents, I_{ON}, I_{diff}, and I_{OFF}. The theoretical values for these thresholds are derived by Nozaki and Delbruck [15], as follows:

$$\theta_{ON} = \frac{\kappa_n}{\kappa_p^2}\frac{C_2}{C_1}\log\left(\frac{I_{ON}}{I_{diff}}\right) \approx \frac{1}{14}\log\left(\frac{I_{ON}}{I_{diff}}\right) \tag{8}$$

and

$$\theta_{OFF} = \frac{\kappa_n}{\kappa_p^2}\frac{C_2}{C_1}\log\left(\frac{I_{diff}}{I_{OFF}}\right) \approx \frac{1}{14}\log\left(\frac{I_{diff}}{I_{OFF}}\right). \tag{9}$$

where $I_{ON/OFF}$ denotes the ON/OFF threshold bias current, I_{diff} is the change amplifier bias current, and $\theta_{ON/OFF}$ represents the ON/OFF threshold.

For the DAVIS-345, the value of the nondimensional term, $\frac{\kappa_n}{\kappa_p^2}\frac{C_2}{C_1}$, can be approximated to be 1/14 [13].

Once an event is detected, the pixel temporarily stops monitoring the change in V_{diff} so that the recording process is done before the next event. The duration of the time that a pixel halts is called the refractory period. The refractory period is uniquely defined by the bias current, I_{refr}. The higher the bias, I_{refr}, is, the shorter the refractory period is. McReynolds et al. established an experimental method to predict the duration of the refractory period and the value was measured to range from $330[\mu s]$to $10[ms]$ [12]. In the astronomical application, the longer refractory period improves the noise performance but increases the possibility that important information is missed. It is also a driver of temporal delays which are asynchronous in different pixels.

In the comparator stage of the simulator, two sources of noise were considered namely leak noise and shot noise. The leak noise is caused by junction leakage and parasitic photocurrent in the reset switch [15, 6]. As it was done in the v2e simulator, the leak noise was modeled by constantly decreasing the memorized reference log-photocurrent:

$$\log I_{ref} = \log I_{ref} - \delta_{leak} \tag{10}$$

where

$$\delta_{leak} = \Delta t f_{leak} \theta_{ON} \tag{11}$$

Δt is the simulation time step, and f_{leak} is the leak noise frequency, which is typically about 0.1 [Hz] [15, 6]. Another source of noise is shot noise, which arises from the quantum nature of photons. In an EV sensor pixel, the rate of shot noise increases as light intensity decreases. Therefore, under low-light conditions, such as when observing objects in space with a telescope, shot noise must be considered. This noise can be modeled by a Poisson process so that the produced noise rate matches the observed noise event rate [6]. More specifically, the observed noise rate, $R_n = 0.05\,[\text{Hz}]$, is scaled by a linear function of the ratio of the current value at the current time to its maximum possible current and a factor F, which is assumed to be 0.25. The scaled noise rate, r, is then multiplied by the time step, δt, to get the probability, p, which is compared with u, a uniformly distributed sample in [0, 1). The maximum possible current is estimated to be 3.16 [nA], calculated from the order of magnitude of the dark current, 1 [fA] [15], and the dynamic range of a typical EV sensor, which is 130 [dB] [14]:

$$r = \left((F-1) \times \frac{I}{I_{max}} + 1 \right) \times R_n \tag{12}$$

$$p = r \times \delta t \tag{13}$$

$$\text{if} \;\; u < p : \text{OFF event} \tag{14}$$

$$\text{if} \;\; u > (1-p) < p : \text{ON event} \tag{15}$$

2.5 Linear Interpolation

One of the most notable features of an EV sensor is that each pixel monitors changes in brightness and records events asynchronously, meaning that the output of an EV sensor is not in the form of frames. However, if we simulate the motion of targets in fixed time steps, the simulated currents and events would also be in the form of frames. To overcome this issue, Mueggler et al. applied a linear interpolation algorithm between frames so that the timestamps of events detected by each pixel would differ, mimicking the asynchronous nature of an EV sensor [14]. Additionally, the linear interpolation algorithm allows us to simulate events that might be missed in the simulator but could be detected by a real EV sensor, as the time step for frame-based simulation is larger than the time resolution of an EV sensor. As shown in Figure 2, the events generated by linear interpolation do not perfectly align with the real events; however, they follow the real event generation pattern, and the error decreases as the number of frames increases. In the proposed simulator, the values of logarithmic current, y_{events}, that spike events between two frames are computed based on the thresholds and logarithmic current at the frames. During this process, the refractory period after each event is also taken into account. Then, the time for the events is computed by

$$t_{event} = t_1 + \frac{t_2 - t_1}{y_2 - y_1}(y_{event} - y_1) \tag{16}$$

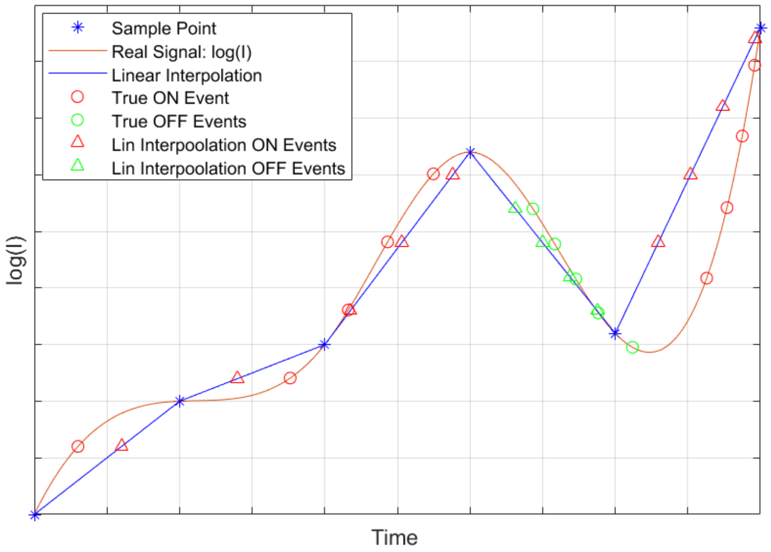

Fig. 2: EV sensor simulation with linear interpolation

2.6 Multi-Pixel Model

The aforementioned process describes how the simulator models the output of a single pixel of an EV sensor. However, to model the output of an entire EV sensor, we need to simulate the output of all pixels. To achieve this, we first simulate the motion of targets within the field of view (FOV). In this paper, the targets are assumed to be point light sources and are modeled using the point spread function given by Equation 17:

Table 1: The bias configuration for the data used for simulator validation

Bias Configuration	I_{pr}	I_{sf}	I_{refr}	I_{ON}	I_{OFF}	I_{diff}
Fast PR, Slow SF, Balanced TH	15.0 μA	834.7 fA	4.7 nA	186.9 nA	2.0 nA	8.2 nA

$$\lambda_{ij} = \frac{\Phi}{4}(erf(\hat{x}_{ij}^{+}) - erf(\hat{x}_{ij}^{-}))(erf(\hat{y}_{ij}^{+}) - erf(\hat{y}_{ij}^{-})) \tag{17}$$

where Φ is the total photon flux reaching the focal plane and $\hat{x}_{ij}^{\pm} = \frac{1}{\sqrt{2}\sigma}(x_{ij}^{\pm} - \bar{x})$ and $\hat{y}_{ij}^{\pm} = \frac{1}{\sqrt{2}\sigma}(y_{ij}^{\pm} - \bar{y})$ are normalized pixel bounds. Note that $\bar{x}$ and $\bar{y}$ are the centroid of the PSF and σ is the standard deviation computed by $0.45\Lambda N$, where Λ is the mean wavelength of the event camera's sensitivity range and N is the telescope f-number. The relationship between Φ and visual magnitude is discussed in [19].

Once we simulate the movement of each target in the FOV over time, we then simulate the time history of light intensity captured by each pixel. From this time history of light intensity, we simulate the photocurrent and generate events for each pixel. To shorten the simulation time, functions that simulate photocurrent over time and generate events are structured to process event history for each pixel, enabling parallel computing for multiple pixels. Figure 3 shows the flow chart of the algorithm.

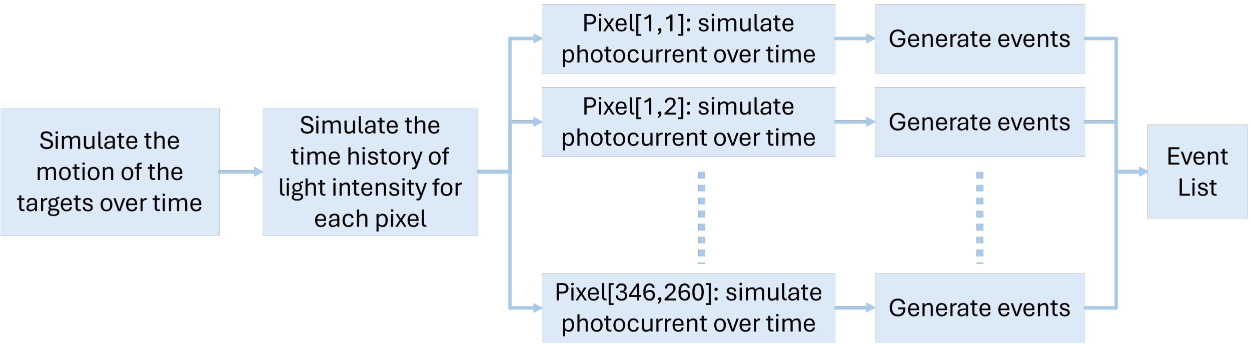
Simulate the motion of the targets over time
Simulate the time history of light intensity for each pixel
Pixel[1,1]: simulate photocurrent over time
Pixel[1,2]: simulate photocurrent over time
Pixel[346,260]: simulate photocurrent over time
Generate events
Generate events
Generate events
Event List

Fig. 3: Simulation algorithm

3. RESULTS

To validate the result of the proposed simulator, the output of the simulator is compared qualitatively and quantitatively with the data taken by the 2nd generation of DAVIS 346.

3.1 Setup

In the proposed simulator, the experiment done by McReynolds et al. [13] was modeled to have some output from real measurements taken by the 2nd generation of DAVIS 346 to compare with. In the study, aligned rotating light sources in a dark room were observed with the DAVIS 346 as shown in Figure 4. The goal of the study was to figure out the optimal bias configuration of EVS for astronomical applications and determine the limitation of the limitation in speed and brightness of the light source that DAVIS 346 can detect in different bias configurations.

The DAVIS 346 is a 346x260 pixels EVS whose pixel size is $18.5\mu m$. The fill factor for the sensor is 22%. Fujinon 7-70mm lens was attached to DAVIS 346, and its focal length and f-number is 41 mm and f/1.8 respectively. The distance from the light sources to the sensor was approximated to be 63 [cm]. The bias configuration of the data we used to validate our simulator was named ”Fast PR, Slow SF, Balanced TH” in the study. Table 2 shows the value of each bias current in the configuration. This bias configuration gives us the ON and OFF threshold of 0.2061 and -0.093 respectively.

In this paper, three scenarios with different bias configurations for the simulator are considered and listed in Table 2. Additionally, the constants necessary for the simulation setup are provided in Table 3.

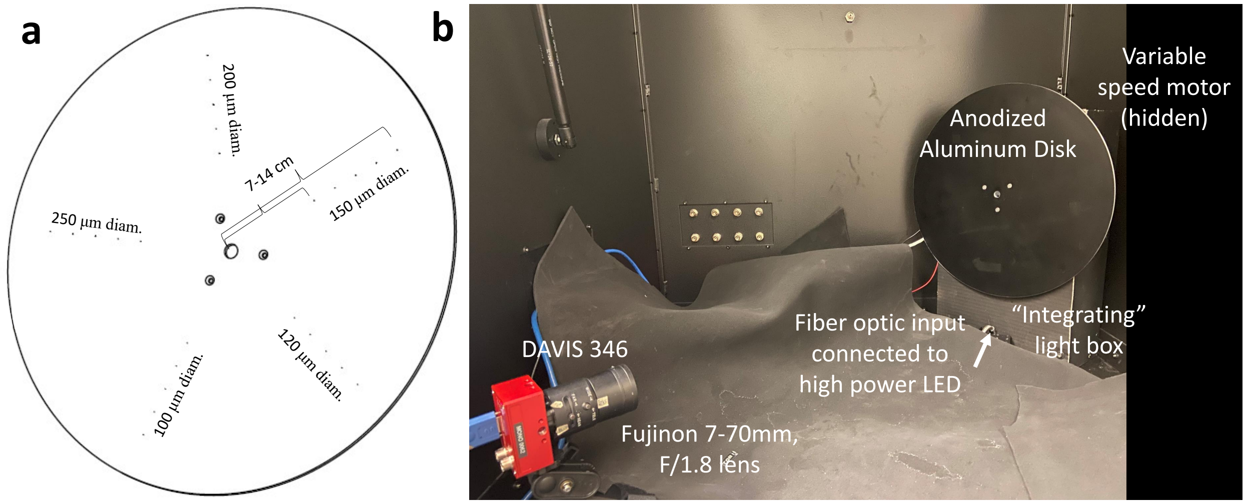

Fig. 4: Experimental lab setup. (courtesy [13])

Table 2: The bias configuration for the data used for simulator validation

No.	Description	I_{ON}	I_{OFF}	I_{diff}	θ_{ON}	θ_{OFF}
1	With the shot noise and leak noise	0.85 μA	69 nA	235.3 nA	0.0846	-0.0809
2	No shot and leak noise, $\lambda_{dark} = 18000e^{-1}/s$	0.85 μA	69 nA	235.3 nA	0.0846	-0.0809
3	No shot and leak noise, $\lambda_{dark} = 290e^{-1}/s$	0.75 μA	0.55 nA	15.03 nA	0.2578	-0.2181

3.2 Qualitative Comparison

One common way to visualize event-based data is to accumulate events over a specific time range to create a ”frame.” Figure 5 shows a comparison of images created by overlaying three successive frames from the real and simulated data. Successive frames are overlaid because it is difficult to see the targets in a single frame. The simulated frame qualitatively matches the real data, effectively capturing the five targets and noise appearance, making it a decent representation of the actual scenario. The integrated frame-based representation of the real and simulated (1 and 3) data are available at the link: Simulation Result

Another visualization method for event data is a 3D scatter plot, where all events are plotted within a 3D volume using the x and y coordinates of the pixels and time. Figure 6 shows the 3D volume plot for the real and simulated data. Due to the linear interpolation between successive frames, the simulated data does not exhibit distinct frames of events. Overall, the simulated data captures the sparseness of the events and the asynchronous behavior of each pixel.

Table 3: Constants in the simulation

Variable	Description	Value	Unit
α	Absorption Coefficient	$3 \cdot 10^{4}$	N/A
η_i	Internal Quantum Efficiency	1	N/A
Φ	Total photon flux in PSF	10^{9}	photons /s
τ	Transmission Coefficient	0.68	N/A
D_h	Hole diffusion coefficient	$6.4632 \cdot 10^{-}4$	m^2/s
D_e	Electron diffusion coefficient	0.0129	m^2/s
e	The electron charge	$.602176634 \times 10^{-19}$	C
fps	Frame rate for position simulation	250	frames/s
L_h	Hole diffusion length	$5.685 \cdot 10^{-6}$	m
L_e	Electron diffusion length	$2.542 \cdot 10^{-5}$	m
n_i	Intrinsic concentration	$2.1 \cdot 10^{12}$	m^{-3}
$N_{a,d}$	Acceptor/dopant concentrations in a semiconductor	10^{23}	m^{-3}
W	Width of the depletion region	$1.1637 \cdot 10^{-7}$	m

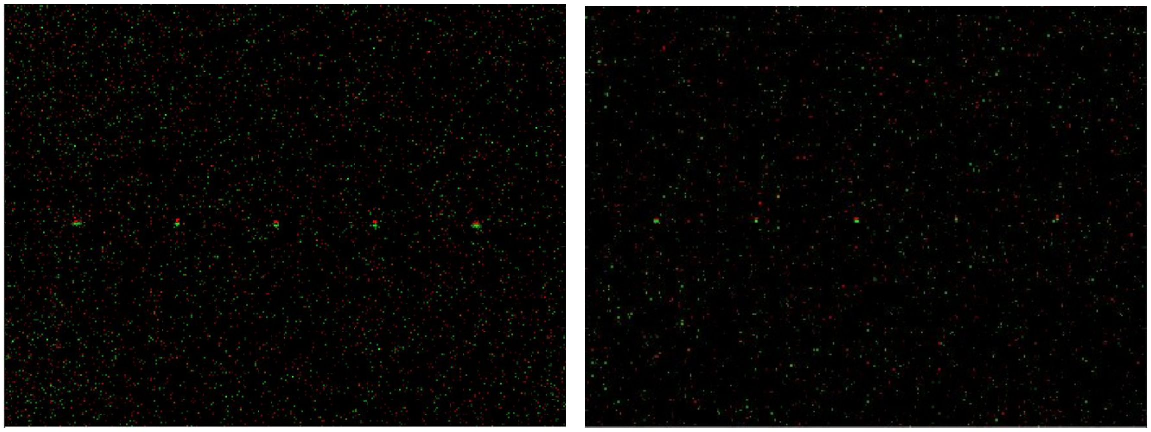

(a) Real Data

(b) Simulated Data

Fig. 5: Overlaied three successive frames created by the real and simulated event data

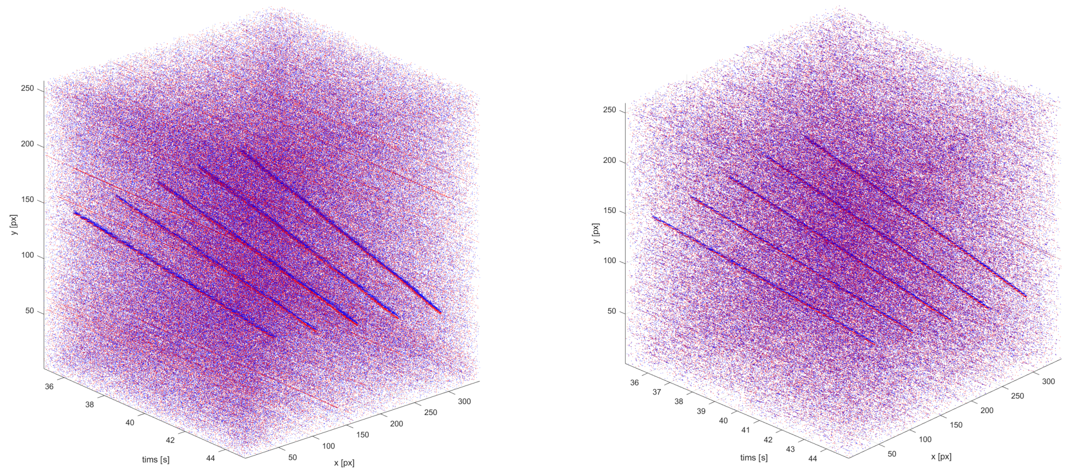

(a) Real Data

(b) Simulated Data

Fig. 6: Overlaied three successive frames created by the real and simulated event data

3.3 Quantitative Comparison

To quantitatively evaluate the simulation, we compared the total number of events and the number of ON/OFF events in the real and simulated event data. Table 4 shows the number of total, ON, and OFF events recorded in the real and simulated data. By tuning the bias current settings and the time-step for simulating the motion of the targets, Simulation 1 successfully generated a similar number of total events and a comparable ON/OFF ratio. However, matching only the number of events and the ON/OFF ratio is not sufficient to fully evaluate the simulator's performance. Since the path of the targets in the simulation is not perfectly aligned with the real data, pixel-by-pixel comparison would be challenging. Therefore, we counted the total number of events generated in each pixel and investigated the distribution of these numbers. Figure 7 shows the histograms of the number of events for the real and simulated data. Since the total number of events in each case is not the same, the frequency is normalized so that only the shape of the distribution needs to be examined. The left and middle columns show the event distribution for the real data and Simulation 1, respectively. The real data has a peak probability in the bin [0, 2], indicating that more pixels recorded between 0 to 2 events throughout the recording. On the other hand, Simulation 1 has a peak around the bin [12, 14] for the total and ON events, and [4, 6] for OFF events. This is because the leak noise causes the sensor to generate ON events at a constant rate, even without a change in photocurrent, making it unlikely for a pixel to have only one or two events in total by the end of the simulation.

We then turned off the leak and shot noise so that we would not get events that were constantly being generated, aiming to match the histograms of the real and simulated data. This resulted in Simulation 2, which generated 541,500 events in total, only 11.7% of the target number. It is clear that simply turning off the shot and leak noise while keeping the same bias current did not resolve the issue. Therefore, the ON and OFF thresholds and the dark current rate were tuned to match the total number of events and the ON/OFF ratio with the real data. This scenario is referred to as Simulation 3. It is worth noting that decreasing the dark current rate from 18,000 $[e^{-1}/s]$ to 290 $[e^{-1}/s]$, meaning fewer free electrons were generated by thermal energy in the photodiode, actually increased the total number of events. This is because, when taking the logarithm of the photocurrent (which includes the dark current) and calculating the difference between the current and memorized log current, a decrease in dark current does not simply lead to a decrease in the total number of events. Simulation 3 generated 4,298,229 events in total, which is close to the real data. The ON/OFF ratio was 0.878, while the real data had a ratio of 0.846. The right column of Figure 7 represents Simulation 3. The peak at the bin [0, 2] can be observed in Simulation 3, and the shape of the histograms is similar to those of the real data. To assess how closely the histograms of the simulated data match those of the real data statistically, we ran the simulation 20 times for Simulation 1 and 3, computed the error for each run by subtracting the histogram of the real data from the one by the simulation, and then took the average of the error in each scenario. Figure 8 shows the percent error in the bin counts between the real and simulated data. The percent error plots for Simulation 1 exhibit a turning point, where the error transitions from positive to negative, or vice versa, particularly in bins with event counts of less than 50. This may be due to pixels recorded in the [0, 2] bin in the real recording, which recorded additional events in the simulation due to leak and shot noise, causing a shift to bins around [10, 12]. There is also a steady percent error for bins with event counts greater than 50. In contrast, the percent error for Simulation 3 is less than that for Simulation 1 in bins with counts of less than 50. Additionally, larger percent errors are observed for bins with counts greater than 50, as the ideal value for this range is small, making the percent error more significant. Figure 9 displays the error in frequency on the left-side y-axis, along with its ratio to the total number of pixels, which is 89,960 ($= 346 \times 260$), providing context for the significance of the error relative to the total number of pixels in the sensor.

Due to the shift in the peak of the histogram, larger errors, around $\pm 10\%$, are observed in bins with smaller event counts. Conversely, as seen from the shape of the histogram in Figure 7 , the error in Simulation 3 is less than 2% of the total number of pixels, which is relatively small. Although Simulation 3 did not include shot and leak noise, its event distribution across the pixels was closer to the real recording than that in Simulation 1. Despite the smaller error, a turning point in the histogram error was observed, which may indicate a bias in the simulator that warrants further investigation in the future.

Table 4: The number of events generated in different settings (see Table 2 for scenario description)

No.	Total events	ON events	OFF events	ON/OFF
Real Data	4628253	2120953	2507300	0.846
1	4589159	2087697	54.51	0.834
2	541500	264302	277198	0.95
3	4298229	2009827	2288402	0.878

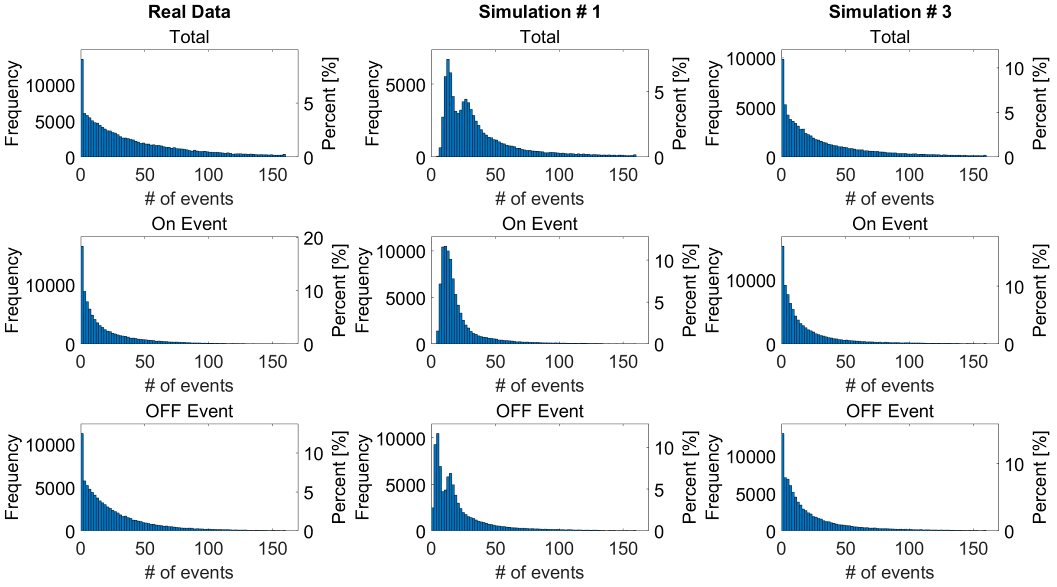

Fig. 7: Event distributions for real and simulated data

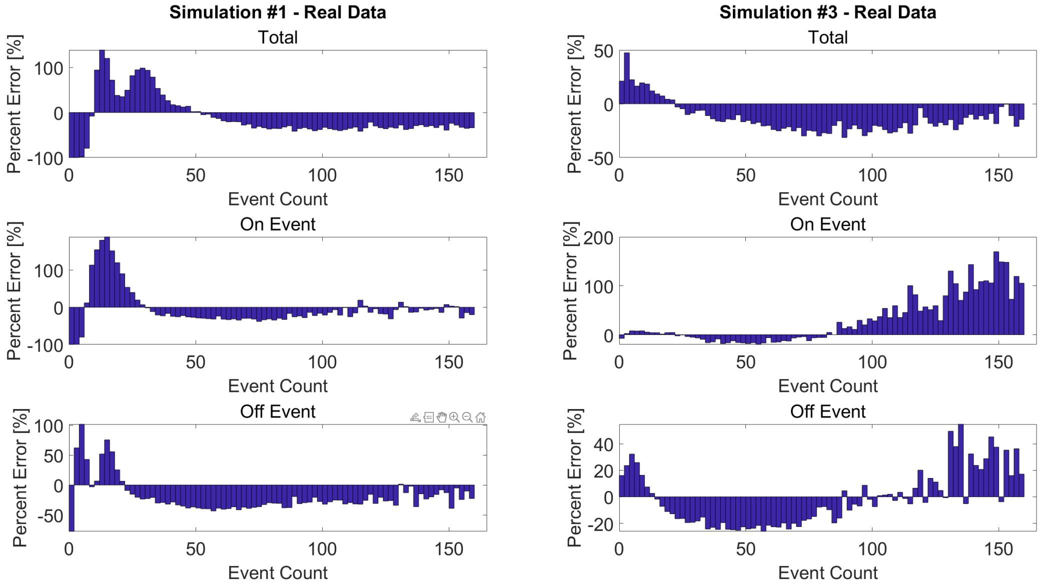

Fig. 8: Percent error in the bin counts of the histogram in Figure 7 against the real data

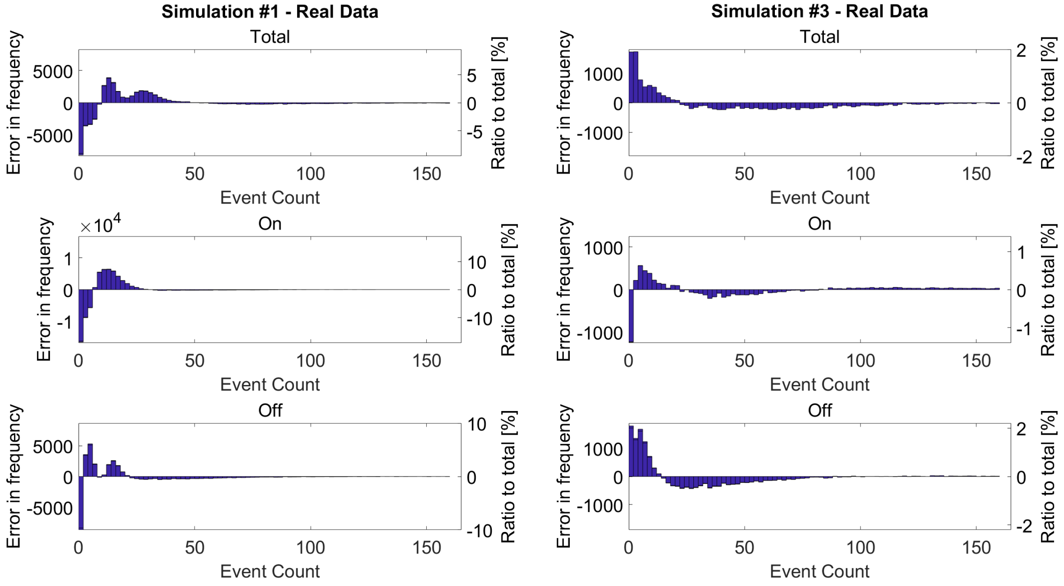

Fig. 9: Error in the bin count and its ratio to the total number of pixels

4. CONCLUSIONS

The proposed EVS simulator successfully models the performance of EVS by considering various physical phenomena and their effects on pixel-level operations. The simulation accurately replicates the characteristics of the DAVIS 346 sensor, incorporating key elements such as photocurrent generation, logarithmic response, noise sources, and asynchronous event detection. The simulation method effectively integrates the modeling of dark current, shot noise, and leak noise, which are critical in low-light conditions such as those encountered in astronomical observations. The qualitative comparisons through frame overlays and 3D scatter plots demonstrate that the simulated data effectively replicates key aspects of the real data, including target visibility and event sparseness. However, despite achieving similar overall event counts and ON/OFF ratios, the quantitative analysis reveals discrepancies in event distribution, highlighting the challenges in perfectly aligning simulation parameters with real-world data. In contrast, a scenario, that excluded leak and shot noises and increased dark current noise, produced an event distribution closer to the real data, with errors less than 2% of the total number of pixels.

5. REFERENCES

[1] Conor J Benson and Marcus J Holzinger. Simulation and analysis of event camera data for non-resolved objects. page 18.

[2] Tat-Jun Chin, Samya Bagchi, Anders Eriksson, and Andre van Schaik. Star tracking using an event camera. In *2019 IEEE/CVF Conference on Computer Vision and Pattern Recognition Workshops (CVPRW)*, pages 1646–1655. IEEE.

[3] Gregory Cohen, Saeed Afshar, Brittany Morreale, Travis Bessell, Andrew Wabnitz, Mark Rutten, and André van Schaik. Event-based sensing for space situational awareness. 66(2):125–141.

[4] Guillermo Gallego, Tobi Delbruck, Garrick Orchard, Chiara Bartolozzi, Brian Taba, Andrea Censi, Stefan Leutenegger, Andrew J. Davison, Jorg Conradt, Kostas Daniilidis, and Davide Scaramuzza. Event-based vision: A survey. 44(1):154–180.

[5] Rui Graça, Brian McReynolds, and Tobi Delbruck. Shining light on the dvs pixel: A tutorial and discussion about biasing and optimization. *2023 IEEE/CVF Conference on Computer Vision and Pattern Recognition Workshops (CVPRW)*, 2023.

[6] Yuhuang Hu, Shih-Chii Liu, and Tobi Delbruck. v2e: From video frames to realistic DVS events. page 10.

[7] Safa Kasap and Ravindra Kumar Sinha. *Optoelectronics and photonics: Principles and practices*. Prentice Hall, 2013.

[8] P. Lichtsteiner and T. Delbruck. A 64x64 aer logarithmic temporal derivative silicon retina. In *Research in Microelectronics and Electronics, 2005 PhD*, volume 2, pages 202–205. IEEE.

[9] P. Lichtsteiner, C. Posch, and T. Delbruck. A 128 x 128 120db 30mw asynchronous vision sensor that responds to relative intensity change. In *2006 IEEE International Solid State Circuits Conference - Digest of Technical Papers*, pages 2060–2069. IEEE.

[10] Patrick Lichtsteiner, Christoph Posch, and Tobi Delbruck. A 128$\times$ 128 120 db 15 μs latency asynchronous temporal contrast vision sensor. *IEEE Journal of Solid-State Circuits*, 43(2):566–576, 2008.

[11] Peter N. McMahon-Crabtree and David G. Monet. Commercial-off-the-shelf event-based cameras for space surveillance applications. *Applied Optics*, 60(25), 2021.

[12] Brian McReynolds, Rui Graca, and Tobi Delbruck. Experimental methods to predict dynamic vision sensor event camera performance. *Optical Engineering*, 61(07), 2022.

[13] Brian McReynolds, Rui Graca, Rachel Oliver, Masashi Nishiguchi, and Tobi Delbruck. Demystifying Event-based Vision Sensor Biasing to Optimize Signal to Noise for Space Domain Awareness. 2023.

[14] Elias Mueggler, Henri Rebecq, Guillermo Gallego, Tobi Delbruck, and Davide Scaramuzza. The Event-Camera Dataset and Simulator: Event-based Data for Pose Estimation, Visual Odometry, and SLAM. *The International Journal of Robotics Research*, 36(2):142–149, February 2017. arXiv:1610.08336 [cs].

[15] Yuji Nozaki and Tobi Delbruck. Temperature and parasitic photocurrent effects in dynamic vision sensors. *IEEE Transactions on Electron Devices*, 64(8):3239–3245, 2017.

[16] Rachel Oliver and Dmitry Savransky. Event-based sensor model for space domain awareness. 2021.

[17] Christoph Posch, Teresa Serrano-Gotarredona, Bernabe Linares-Barranco, and Tobi Delbruck. Retinomorphic event-based vision sensors: Bioinspired cameras with spiking output. 102(10):1470–1484.

[18] Behzad Razavi. *Design of analog CMOS integrated circuits*. Mcgraw-Hill Education (India) Private Limited, 2020.

[19] James R Shell. Optimizing orbital debris monitoring with optical telescopes. Section: Technical Reports.

6. ACKNOWLEDGMENT

I would like to express my deepest gratitude to Prof. Tobias Delbruck from the Institute of Neuroinformatics, University of Zurich/ETH Zurich, for his invaluable guidance and support. His expertise in neuromorphic engineering and event-based vision sensors has been instrumental in shaping my understanding and the development of this work.